ORIGINAL ARTICLE

Synergistic effects of specimen dimensions and curing regimes on mechanical, physical, microstructural properties and high-temperature performance of alkali-activated mortars

Enes Ekinci · Fatih Kantarcı

Received: 18 July 2025 / Revised: 11 September 2025 / Accepted: 26 April 2026
© The Author(s) 2026

Abstract
This study systematically investigates the synergistic effects of specimen dimensions and curing regimes on the mechanical, physical, microstructural, and high-temperature properties of alkali-activated mortars (AAMs). AAMs were prepared by mixing aggregates with ground granulated blast furnace slag, and activated with 10 M NaOH solution. These mixtures were cast into moulds of three different specimen dimensions ($5 \times 5 \times 5$ cm, $10 \times 10 \times 10$ cm, and $15 \times 15 \times 15$ cm) and cured under three distinct curing regimes (ambient laboratory conditions, water curing, and outdoor winter exposure. The experimental program focused on the high-temperature performance of AAMs, as well as strength, water absorption, fracture analyses. In addition, the microstructural characteristics of AAM specimens were examined using by Scanning Electron Microscopy coupled with Energy Dispersive X-ray Spectroscopy, X-ray Diffractometry, and Fourier Transform Infrared Spectroscopy analyses. The results demonstrated that larger specimen dimensions and water curing substantially improved compressive strength (exceeding 50 MPa at 28 days) and reduced water absorption (<4%), while outdoor curing led to poor performance. Moreover, after exposure to 750 °C, it was observed that larger water-cured specimens maintained higher residual strength and a denser aluminosilicate matrix with fewer cracks. Overall, this study contributes to the potential applications of AAMs by highlighting their suitability for prefabricated and fire-resistant elements, while also providing a novel perspective by demonstrating that AAM's compressive behavior cannot be fully explained through fracture behavior of traditional Portland cement based composites.

Keywords Alkali activated materials · Fire resistance · Microstructure · Curing condition · Mechanical properties

1 Introduction

Portland Cement (PC) production has destructive environmental impacts, primarily caused by the calcination of $CaCO_3$ and the combustion of fossil fuels required to generate the high temperatures needed in the kiln [10]. While the 27 subcategories of PC, classified under the 5 main types (CEM I to CEM V), differ in the proportion

Published online: 03 June 2026

of their main components, all contain clinker as a main component [45]. Even with initiatives like using eco-friendly fuels [39] or adopting energy-saving technologies [28], the calcination of $CaCO_3$, the primary component of clinker, will continue to produce CO_2. It was estimated that about 0.65–0.92 tons of CO_2 emissions are generated from 1 ton of PC production in a cement plant equipped with modern technology, depending upon the clinker/cement ratio [40]. When these ratios are considered alongside the fact that building a typical family home requires 14 tons of PC or that one kilometer of highway contains up to 2500 tons of PC [13], it becomes evident how significantly PC production can impact the environment. These alarming facts have motivated scientists, particularly in recent years, to explore alternative materials to replace PC. Perhaps the most promising of these alternative materials are alkali-activated materials (AAMs) and geopolymers, which not only reduce CO_2 emissions but also effectively recycle industrial by-products.

AAMs have shown to be sustainable alternatives to their traditional PC counterparts. AAMs not only cause less CO_2 emissions during production, but also provide economic and environmental benefits by converting blast furnace slag, an industrial by-product, into a value-added product provides [18, 38, 46, 47]. Slag, a by-product of iron and steel factories, has a global average annual production more than 500 million tonnes, although most of the slag produced has not been used effectively [36]. The usage of slag, which reaches such high production volumes, in the production of concrete can not only minimize problems caused by PC, but also contribute to the concept of circular economy. Alkali activated slag (AAS) is a high-performance building material formed by a series of chemical reactions between alkali activators and slag [6, 25, 49]. Although generally promising results have been achieved in alkali-activated systems and geopolymer composites against chemical attacks and high-temperature effects [23, 33], it should be underlined that performance criteria are directly affected by the binder selection. Contrary to the relatively weak sodium aluminosilicate gel occured as a result of the geopolymerization reaction of raw materials with low Ca content (fly ash and metakaolin) [16], the formation of CSH gel with low porosity and high strength is observed as a result of alkali activation of slag with high Ca content [41].

Adjusting the curing conditions (temperature, humidity and duration) plays a critical role in analysing the microstructure of geopolymer mortar and hence its mechanical and high temperature performance [22]. Elevated curing temperatures generally accelerate the geopolymerization process, leading to enhanced early-age strength, while ambient temperature curing offers a more practical approach for cast-in-situ applications, eliminating the energy-intensive requirements of heat curing. The optimization of curing parameters is required to adapt the properties of geopolymer materials for specific engineering applications [9]. High temperature performance is an important issue for structural materials and applications. Geopolymer binders exhibit superior thermal stability in comparison with ordinary PC concrete (PCC), due to inorganic polymeric structure which does not contain hydration of calcium silicate phases. Geopolymer materials undergo a series of complex physical and chemical transformations, including dehydration, decomposition, and phase transitions after subjected to high temperatures. It may affect structural stability and mechanical integrity.

There are some issues that prevent the effective use of geopolymer materials or alkali-activated binders as an alternative to traditional PCCs [29]. Establishing general standards will only be possible by highly efficient investigations, which can be achieved by further investigating the mechanical and durability performances of AASs under different curing conditions and at different sample dimensions. Although there are studies separately investigating the effects of curing conditions and specimen dimensions on GPCs, there is no study that systematically investigates the synergistic effects of specimen dimensions and realistic curing conditions on mechanical, physical, microstructural properties and high-temperature performance of AAMs. This experimental study was conducted to explore synergistic effects of various sample dimensions and curing conditions on the performance of AAMs.

Table 1 The chemical content of GGBFS

GGBFS	CaO	SiO_2	Al_2O_3	SO_3	Fe_2O_3	$Na_2O_+K_2O$	Mn_2O_3	TiO_2	MgO	LOI
Content, (%)	32.45	32.47	9.94	0.82	1.25	1.16	3.51	1.16	9.31	3.6

Table 2 Physical and chemical properties of NaOH

	Sodium hydroxide
Chemical formula	NaOH
Solubility, (g/l)	1110 (at + 20 °C)
Molecular mass, (g/mol)	39.997
Density, (g/cm^3)	2.13
Acidity	Very low (pH 13–14)
Colour	White
Freezing point, (°C)	14
Melting point, (°C)	318
Boiling point, (°C)	1390

Table 3 Physical characteristics of river aggregates

	River aggregates	
	0–2 mm	2–4 mm
24-h water absorption, (%)	2.62	2.06
Saturated surface dry specific gravity	2.42	2.49
Dry specific gravity	2.36	2.44

2 Materials and methods

2.1 Materials

2.1.1 Ground granulated blast furnace slag (GGBFS)

GGBFS, which was supplied from Karçimsa Cement Industry, was used as raw material for the fabrication of AAM specimens. The chemical composition of GGBFS is presented in Table 1. The specific gravity of GGBFS is 2.86, and the Blaine value is 3870 cm^2/g.

2.1.2 Sodium hydroxide

The highly alkaline environment required for alkali activation reactions was provided using a 10 M NaOH solution. In this study, NaOH with 98% purity was used. Drinkable tap water, compliant with the TS EN 1008 standard [43] , was utilized for preparing the solution, and no additional water was added to the AAM mixture apart from the solution. Some of the physical and chemical properties of the NaOH used in this study are presented in Table 2.

2.1.3 Aggregate

The river aggregates, which were tested for their suitability, were utilized in AAM production by mixing in equal proportions with particle sizes of 0–2 mm and 2–4 mm. Some physical properties of these aggregates used in experimental studies were obtained according to TS EN 1097-6 standard [44] and are presented in Table 3.

2.2 Methods

2.2.1 Mixture types and experimental parameters

This study investigates the effects of environmental curing conditions and specimen dimensions on the mechanical, physical, and microstructural properties, as well as the high-temperature performance, of AAM. For this purpose, cubic AAM specimens with dimensions of 5 × 5 × 5 cm, 10 × 10 × 10 cm, and 15 × 15 × 15 cm were produced and cured under three different conditions (laboratory environment, water, and outdoors during the winter season). The influence of specimen dimensions and curing conditions on the mechanical, physical, and microstructural characteristics, as well as the high-temperature performance of AAMs, was systematically examined.

2.2.2 Mixture proportions

In this study, 10 M NaOH solution was used as alkali activator. To ensure optimum workability of AAM mixtures, the alkali activator solution-binder ratio was experimentally adopted as 0.55 and the binder-aggregate ratio was determined as 2. No extra water was added to the mixture except for the alkali activator solution. For each formulation, three specimens were prepared and tested, and the average values are reported along with the standard deviations.

2.2.3 Mixing, placing and curing condition

The mixture was prepared by first blending aggregates with particle sizes of 0–2 mm and 2–4 mm in equal proportions 3 min. Subsequently, GGBFS was added in the predetermined ratio and mixed until a homogeneous mixture was achieved. Finally, an alkali activator solution, prepared at a 10 M concentration and allowed to rest, was gradually added while mixing. The fresh AAM mixture was then poured into molds with dimensions of 5 × 5 × 5 cm, 10 × 10 × 10 cm, and 15 × 15 × 15 cm. The specimens were cured under laboratory conditions, in a water environment, and outdoors during the winter season. The temperature variations and humidity values of the outdoor curing conditions are presented in Fig. 1. The specimens cured in water were kept in a curing tank maintained at a constant temperature of 23 °C. For the laboratory-cured specimens, the ambient temperature was set at a constant 23 °C, and the relative humidity was measured to be approximately 55%. Dimensions, curing conditions and mixture proportions of AAMs are presented in Table 4.

2.2.4 Experimental tests

The influence of specimen dimensions and curing conditions on the physical, mechanical, and microstructural characteristics, as well as the high-temperature performance, of AAMs was systematically investigated. The

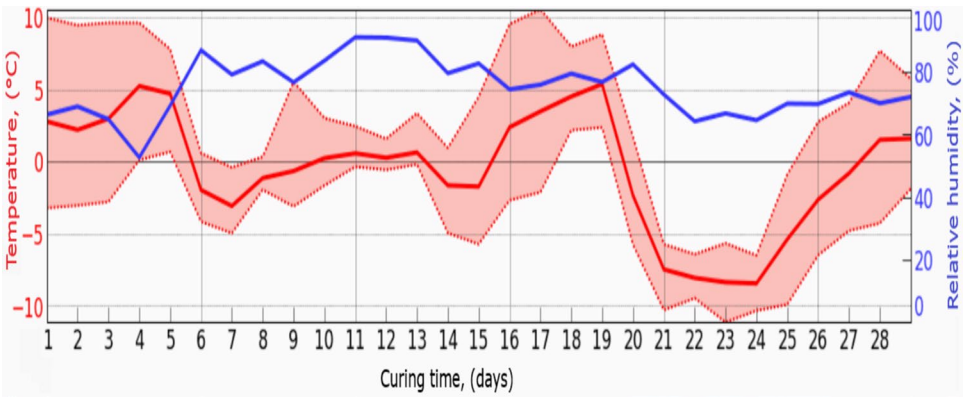


Fig. 1 The temperature variations and humidity values of the outdoor curing

Table 4 Dimensions, curing conditions and mixture proportions of AAMs

No	Mix ID	Sample dimension, (cm)	AAM ingredients, (g)			Curing regime		
			GGBFS	NaOH	Aggregate	Ambient	Outdoor	Water
1	5-A	5 × 5 × 5	600	330	1200	✓		
2	5-O	5 × 5 × 5	600	330	1200		✓	
3	5-W	5 × 5 × 5	600	330	1200			✓
4	10-A	10 × 10 × 10	4800	2640	9600	✓		
5	10-O	10 × 10 × 10	4800	2640	9600		✓	
6	10-W	10 × 10 × 10	4800	2640	9600			✓
7	15-A	15 × 15 × 15	16,200	8910	32,400	✓		
8	15-O	15 × 15 × 15	16,200	8910	32,400		✓	
9	15-W	15 × 15 × 15	16,200	8910	32,400			✓

Table 5 The experimental parameters and test of AAMs

Experimental parameters		Tests
Cubic sample dimensions (cm)	Curing conditions	
5 × 5 × 5 10 × 10 × 10 15 × 15 × 15	Laboratory Water Outdoor in winter	Mechanical properties (3, 7 and 28-day compressive strength, crack patterns)
		Physical properties (apparent porosity, water absorption)
		Microstructure properties (SEM–EDX)
		Elevated temperature performance (changes in compressive strength and weight, visual appearance, water absorption, and SEM–EDX, XRD, FTIR analysis)

experimental parameters and tests performed in this study are comprehensively presented in Table 5 and Fig. 2. The compressive strength tests were performed according to ASTM C109 standard [2] and results represent the average of three independent measurements. Apparent porosity and water absorption tests carried out in compliance with ASTM C642 [4]. Furthermore, microstructure analyses were conducted using the LEO-EVO 40 type Scanning Electron Microscopy (SEM) apparatus in compliance with ASTM C1723 standard [3] . The chemical compositions of AAMs were defined with Energy dispersive X-ray (EDX) analyses. X-ray Diffractometry (XRD) analysis was performed to identify the phases present in the AAM samples. The Fourier Transform Infrared Spectroscopy (FTIR) analyses of the AAM specimens were conducted in accordance with ASTM E1252 [5].

3 Results and discussion

3.1 Compressive strength of AAM samples

3.1.1 Effect of specimen dimension

Compressive strength values of the AAM samples at 3, 7, and 28 days are presented in Figs. 3, 4 and 5, respectively. The experimental findings revealed that an increase in specimen dimension positively influenced compressive strength at all specimen ages. At 3 days, compressive strength increased significantly with specimen dimension across all curing regimes; in water-cured AAMs, the 5 × 5 × 5 cm specimen reached 16.5 MPa, rising to 19.8 MPa for 15 × 15 × 15 cm.This increase was also observed under the other curing regimes. Under outdoor curing, inadequate conditions (destructive weather) yielded low strengths (3.5–6 MPa) across all dimensions. Consistent with the 3-day results, at 7 days the 15 × 15 × 15 cm water-cured specimens exceeded 25 MPa, while

 https://doi.org/10.1007/s43452-026-01540-3

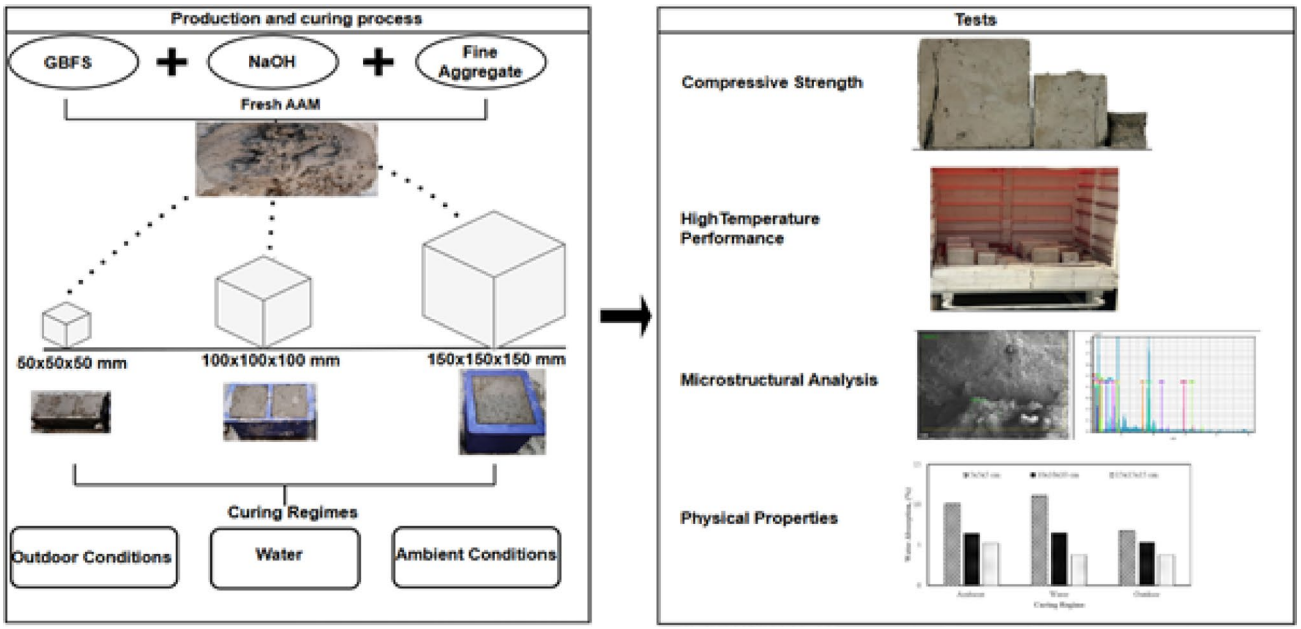
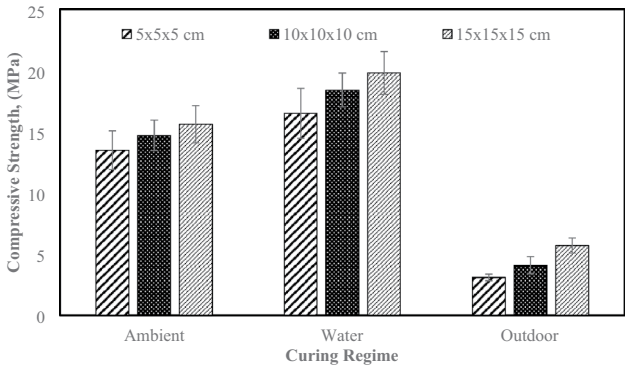


Fig. 2 Flowchart of the experimental procedure

Fig. 3 Compressive strength values of the AAM samples at 3 days



the 5 × 5 × 5 cm specimens were about 35% lower at 17.3 MPa. Furthermore, at 28 days, the trend of higher strength with increasing specimen dimension persisted. As shown in Fig. 5, increasing size from 5 × 5 × 5 cm to 15 × 15 × 15 cm raised strength by approximately 113%, 111%, and 150% under ambient, water, and outdoor curing, respectively. These findings indicate that the dimension effect on AAM's compressive behavior cannot be fully explained by fracture-mechanics theories for conventional PC-based composites. In PC-based systems, microcracks typically initiate at the weak interfacial transition zone (ITZ) and rapidly propagate through the heterogeneous matrix. By contrast, in geopolymers the continuity and homogeneity of the gel dominate crack initiation and propagation [11]. These notable findings indicate that the dimension effect on the compressive behavior of geopolymer binders cannot be fully explained by the fracture mechanics theories developed for conventional PC-based composites. As is well known, microcracks in conventional PC-based composites typically initiate at the weak ITZ and propagate rapidly through the heterogeneous matrix, leading to fracture. However, as emphasized by Duxson et al. [11], the continuity and homogeneity of the gel structure in geopolymer binders play a dominant role in crack initiation and propagation under stress. In this context, a detailed focus on the mixing ratios would provide valuable insights. In this study, AAM mix proportions (GGBFS:aggregate:NaOH solution) were 1:2:0.5. These ratios indicate a relatively high aluminosilicate gel content, and SEM confirmed a compact, homogeneous, densely structured gel phase. It is considered that the high continuity and density of

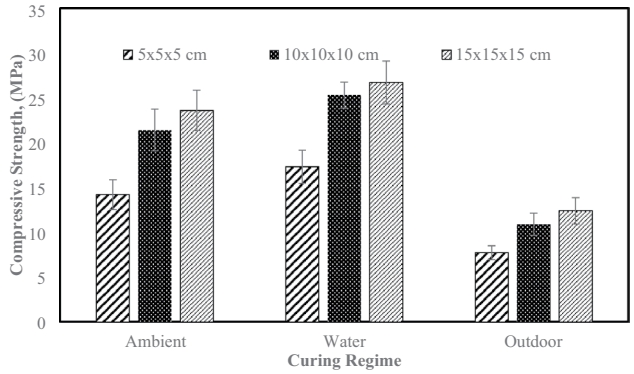


Fig. 4 Compressive strength values of the AAM samples at 7 days

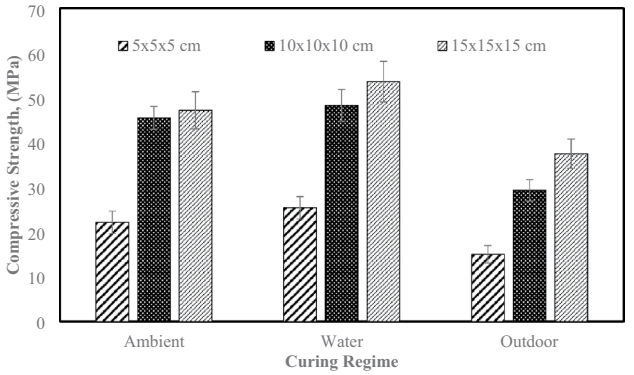


Fig. 5 Compressive strength values of the AAM samples at 28 days

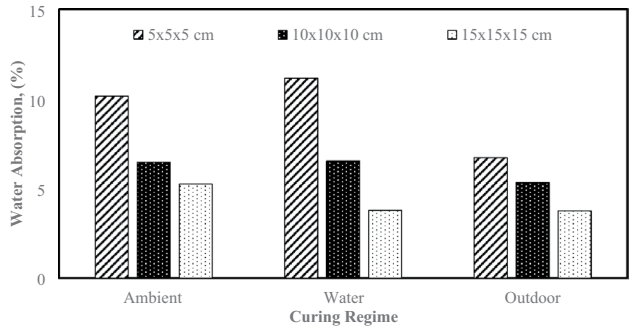


Fig. 6 Water absorption values of the AAM samples

the geopolymer gel structure might delay crack initiation and limit crack propagation. Angular cracking was observed in large samples, while limited fracture behaviour was observed with defined granular fragmentation in small samples. Unlike ordinary PC-based composites where increased specimen dimension often leads to reduced mechanical performance, AAMs with a high binder phase exhibited an increase in compressive strength with larger sample dimensions. Similarly, Zhang et al. [50] stated that C–(N–)A–S–H gel structures with a higher Ca/Si ratio offer greater resistance to crack initiation and propagation.

3.1.2 Effect of curing regime

The effect of three curing regimes on compressive strength was evaluated at 3, 7, and 28 days. The results showed that curing conditions critically influenced mechanical performance at both early and later ages. As shown in Fig. 3, water-cured AAM samples exhibited the highest compressive strength across all specimen dimensions, followed by those cured under ambient and outdoor conditions, respectively. This trend persisted at both 7 and 28 days, with water-cured AAM specimens consistently outperforming those cured under ambient and outdoor conditions across all testing ages. For $15 \times 15 \times 15$ cm AAM specimens, replacing water with outdoor curing reduced compressive strength by approximately 70%, 53%, and 30% at 3, 7, and 28 days, respectively. Percentage findings on the effects of curing regimes on compressive strength values revealed that the curing regime had more pronounced effects, especially at early ages. Despite the unfavorable outdoor conditions, the slow developing reactions gradually contributed to the development of strength at later ages, reducing the initial large percentage differences in compressive strength. On the other hand, obtaining high compressive strength values by applying the water curing regime actually shows that GGBFS-based geopolymer differ from the classical

geopolymer definition in some respects. Unlike typical low-calcium geopolymer, it was speculated that the water curing in slag-based geopolymer systems results in higher mechanical characteristics due to the hydraulic nature of GGBFS and its ability to form C–A–S–H and N–C–A–S–H type hybrid gels under moist conditions, enhancing strength development. Previous studies likewise reported that water curing significantly improves the mechanical properties of GGBFS-based composites [37] and is the most advantageous condition for physico-mechanical properties [7].

3.2 Water absorption of AAM samples

Figure 6 presents water absorption values of AAM samples with different dimensions and curing conditions. Smaller specimens exhibited higher water absorption across all curing regimes. For instance, in ambient-cured specimens, the water absorption ratio of 5 × 5 × 5 cm AAM samples was determined as 10.15%, whereas specimens with dimension of 10 × 10 × 10 cm and 15 × 15 × 15 cm exhibited lower water absorption values of 6.47% and 3.78%, respectively. Additionally, similar trends were observed other samples cured in water and outdoor. It was speculated that this situation is due to the high surface area/volume (SA/V) properties of small samples compared to larger counterparts. Namely, the SA/V ratio of the 5 × 5 × 5 cm AAM specimens is 1.2, whereas this ratio decreases to 0.4 in the 15 × 15 × 15 cm specimens. It is thought that this significant difference indicates that in larger samples, it will be quite difficult for water to penetrate into the inner regions, thus decreasing water absorption values.

In larger samples, the higher water absorption observed in ambient-cured AAMs is attributed to increased water evaporation from the larger exposed surface area in a dry environment. It was speculated that the intense evaporation can enhanced the water absorption capacity by the formation of rough surface structure. On the other hand, the outdoor curing conditions might have slowed down the kinetics of geopolymerization reactions, resulting in insufficient gel formation and irregular pore structure. This may have resulted in an insufficient aluminosilicate gel network and a discontinuous, irregular pore structure. Additionally, low evaporation under outdoor conditions reduced water absorption by preventing the formation of surface microcracks. Consequently, samples with high compressive strength may not always show low water absorption values. Significant relationship between strength and permeability cannot always be found and that these two properties are determined by different microstructural mechanisms (Fig. 7).

3.3 Crack patterns of the AAM specimens

The fracture patterns observed after the compressive strength tests clearly revealed that the curing regime and sample dimension are effective in combination on the mechanical characteristics and fracture behaviour of GGBFS-based AAM specimens (see Table 6). For instance, the highest compressive strength values were obtained in all dimensions in the samples cured in water, and brittle fracture characteristics were observed especially in larger samples. In addition, the sharp, distinct crack formations observed in the 15 × 15 × 15 cm samples indicated the

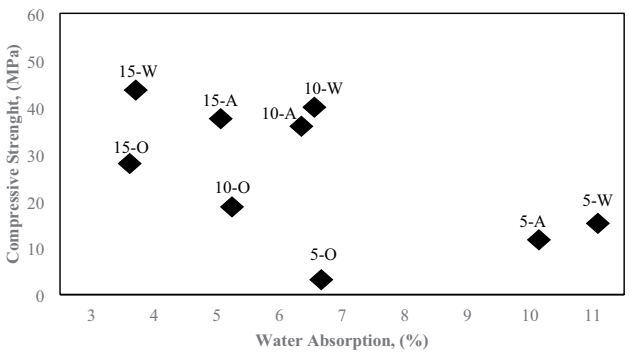


Fig. 7 Correlation between compressive strength and water absorption values

Table 6 Crack patterns of AAMs before and after loading

Curing Condition	Before Loading	After Loading
Ambient		
Water		
Outdoor		

presence of a dense and rigid aluminosilicate matrix developed under constantly humid conditions. On the other hand, outdoor-cured samples where the lowest strengths were obtained showed more irregular fracture surfaces with minimal cracks; however, small specimens exhibited marked fragmentation and disintegration. In summary, the fracture morphologies of the AAM specimens were consistent with the compressive strength results; curing conditions and specimen dimension significantly affected not only strength development but also the fracture behaviour of geopolymer systems. As can be seen from Table 6, fracture patterns in larger dimensions of AAM samples appeared as peelings on the side parts as a result of cracks propagating from top to bottom on the surfaces. In contrast to the larger specimens, shear planes were formed and granular fragmentation was observed in the $5 \times 5 \times 5$ cm specimens due to the concentration of stresses in small volumes. Zhang et al. [50] investigated the fracture patterns of geopolymers samples different dimensions. In line with our observations, researchers stated that vertical cracks formed in larger samples and fragmentation was observed in smaller specimens [50]

3.4 Microstructural analysis

3.4.1 SEM analysis

3 and 28-day SEM observations of AAM samples produced in different dimensions and kept under different curing conditions are presented in Figs. 8 and 9, respectively. These observations revealed that the microstructure of $15 \times 15 \times 15$ cm AAM samples improved significantly between the 3rd and 28th days and the cracks decreased significantly. This microstructural development also showed itself with the densification of the aluminosilicate gel and the significant decrease in the ratio of unreacted GGBFS particles. For instance, Fig. 8a–c shows the formation of visible cracks, pores, and unreacted GBFS particles in the 3-day specimens, while Fig. 9a–c exhibited a much denser and more compact microstructure at the end of 28-day. These microstructural developments indicate that the reactions in the AAM specimens significantly progressed with increasing curing time. Especially in the samples subjected to water curing, it was observed that the microstructural evolution that allowed the formation of a very compact structure was developed by ensuring the continuity of alkali activation. As seen in Fig. 8d, even at the 3-day cure time, the water-cured specimen exhibits the development of continuous gel phases with fewer

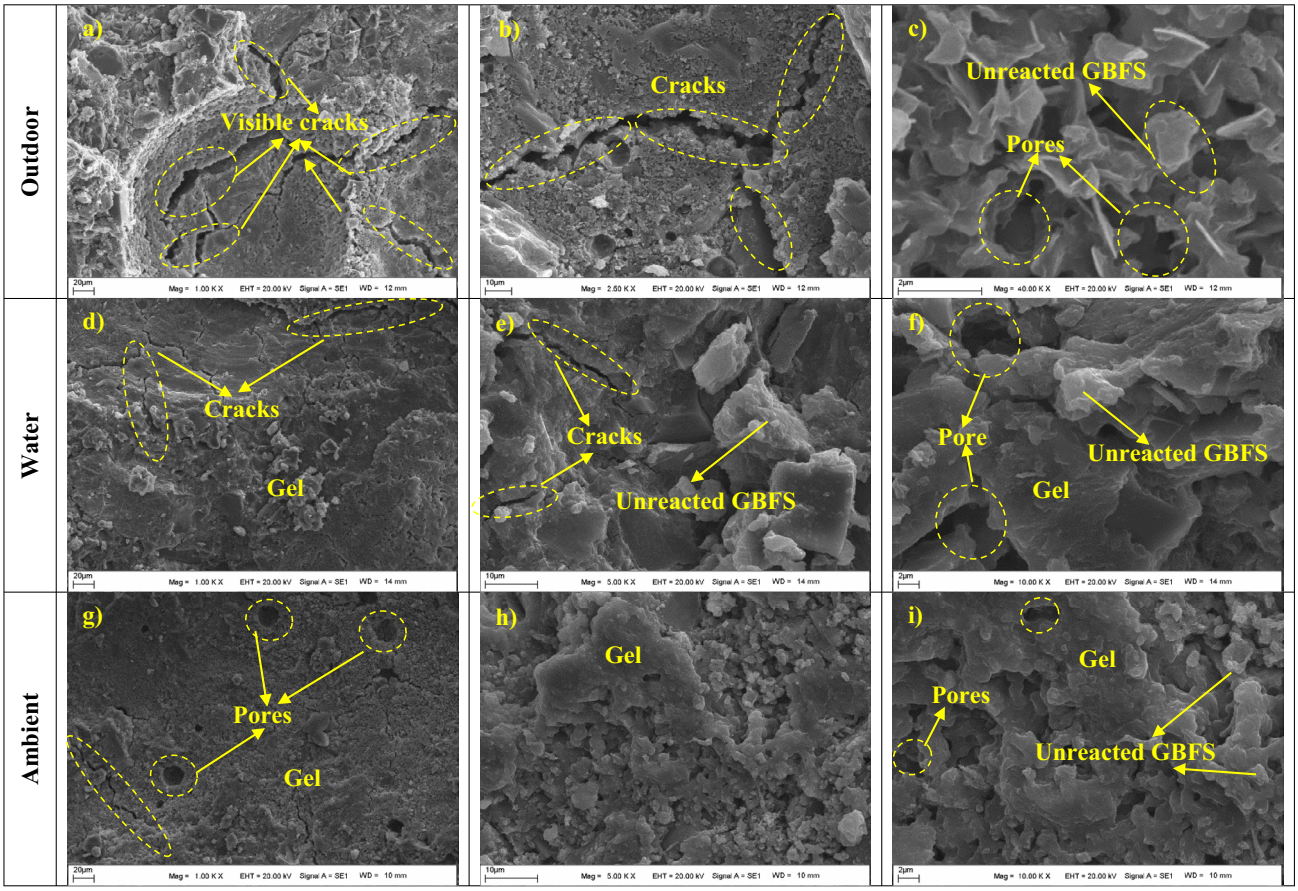


Fig. 8 SEM images of 3-day AAM specimen

microcracks, while the outdoor-cured specimen in Fig. 8a exhibits numerous visible cracks and a more porous microstructure. This process, which resulted in a crack-free and compact microstructure, as seen in Fig. 9d–f, exhibited a consistent attitude with compressive strength values exceeding 50 MPa and water absorption values below 4% on the 28th day in the water cured samples. On the other hand, comparing Figs. 8a and 9a, it was also determined that the cracks observed on the 3rd day in the samples cured under outdoor conditions did not close completely even on the 28th day, and that outdoor curing conditions led to the production of a sample with higher porosity and lower compressive strength. These findings revealed that curing conditions and specimen dimensions directly affect geopolymerization processes and have a significant effect on the ultimate performance criteria. As a result, it was determined that curing regime and specimen dimension optimizations should be considered together for the production of AAMs with superior structural properties.

3.4.2 EDX analysis

EDX analysis results show that the curing duration and conditions of 3- and 28-day AAMs have significant effects on the elemental composition (Figs. 10, 11). It is particularly striking that the Si and Al ratios were high in the 3-day-old samples at ambient cure. These high ratios may indicate that a highly efficient polycondensation reaction took place at early ages under ambient conditions. On the other hand, the fact that the Na, Ca and Al ratios were higher in the samples with water curing in the first days allowed us to comment on the high diffusion of the activator solution and the integration of dissolved ions into the environment to form a geopolymer structure. In water-cured samples, higher Ca content indicated the presence of calcium-rich reaction products.

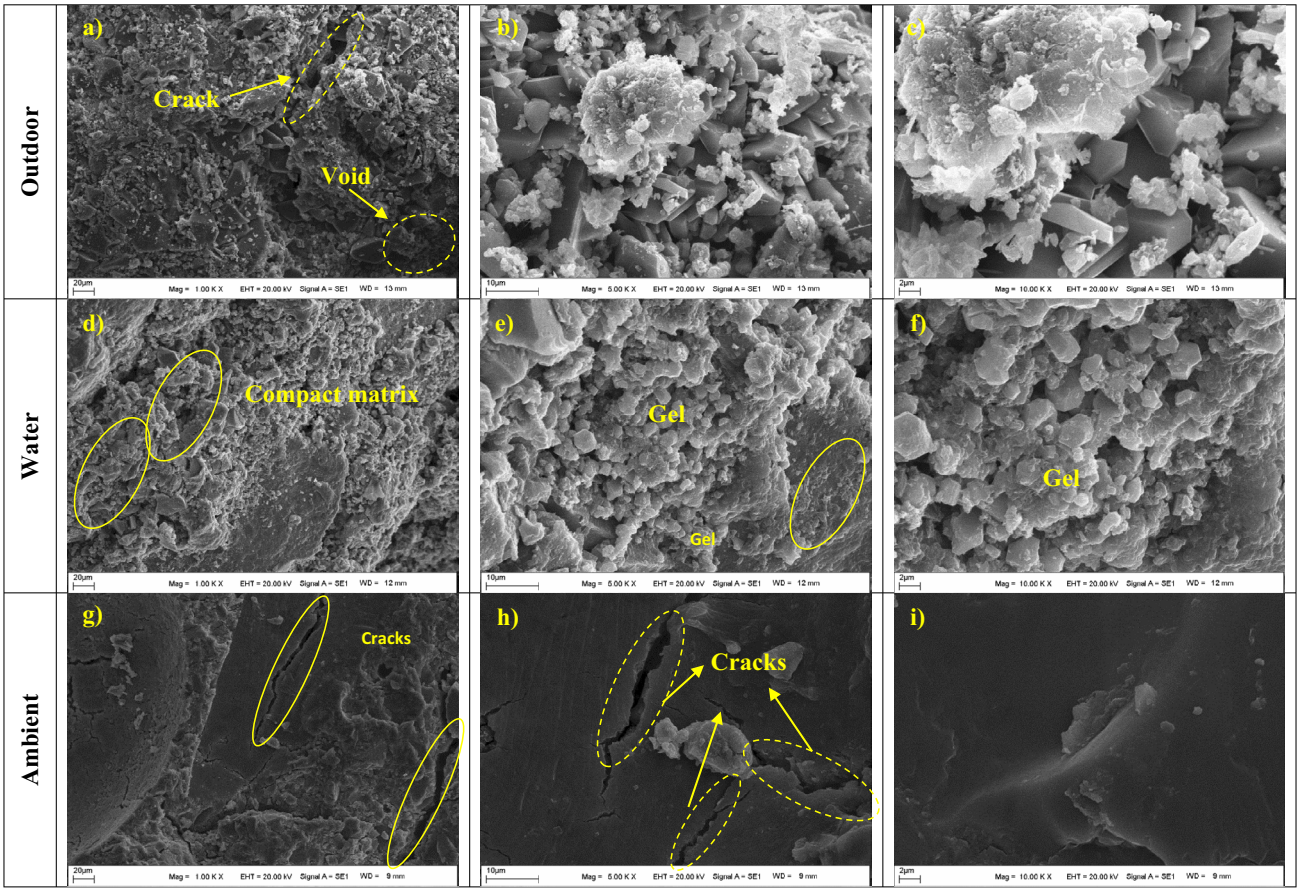
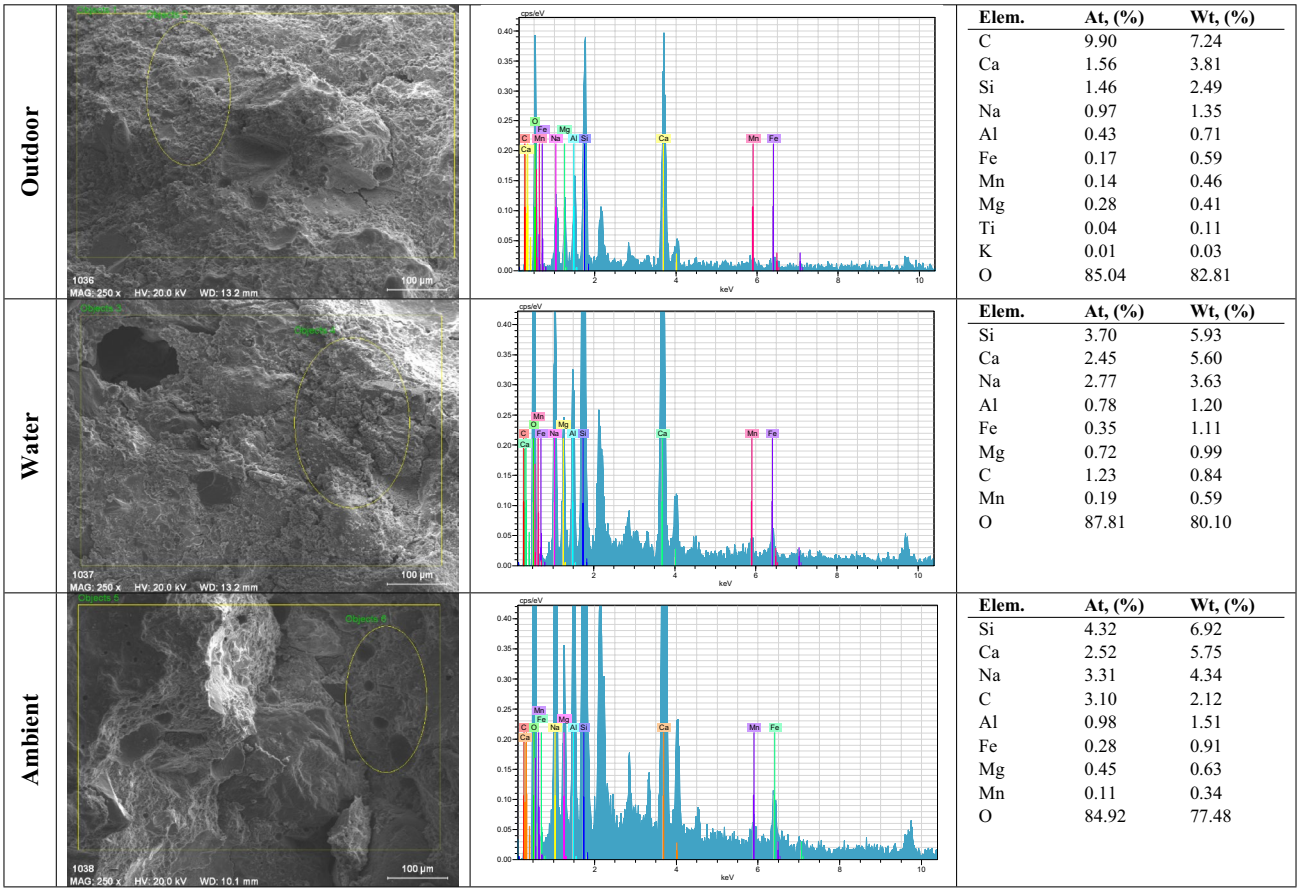


Fig. 9 SEM images of 28-day AAM specimen

The observation of high Ca in water cured samples supported the formation of C–A–S–H gels resulting from the usage of blast furnace slag in addition to traditional N–A–S–H gels. The formation of C–A–S–H gels in addition to N–A–S–H gels confirms the higher compressive strength values observed due to water curing, indicating that water curing is highly effective in GBFS-based AAM.

3.4.3 XRD analysis of AAM specimens

The XRD analyses of AAM specimens based on the curing conditions are presented in Fig. 12. The XRD patterns of AAM specimens cured under different conditions (ambient, water, and outdoor) revealed distinct phase formations influenced by the curing regime. Diffraction peaks attributed to silicon oxide (SiO_2), paragonite ($NaAl_2(Si_3Al)O_{10}(OH)_2$) and C–S–H (Calcium silicate hydrate) were detected in the AAM samples. The C–S–H peak, which was detected sharper and more intensely in the water-cured sample, is attributed to the enhanced geopolymerization and crystal phase development due to availability of water, which promotes gel formations [24]. In contrast, the ambient (15-A) and outdoor (15-O) cured samples exhibited more prominent silicon oxide and paragonite peaks. This is attributed to the presence of unreacted crystalline silica and secondary sodium-aluminosilicate phases, probably resulting from incomplete reaction. The presence of unreacted quartz is typical in geopolymer systems. It is considered an inert residual phase from the raw material [12]. These results demonstrate that curing conditions significantly influence phase formation, crystallinity, and thus the microstructural integrity of AAMs.



Elem.	At, (%)	Wt, (%)
C	9.90	7.24
Ca	1.56	3.81
Si	1.46	2.49
Na	0.97	1.35
Al	0.43	0.71
Fe	0.17	0.59
Mn	0.14	0.46
Mg	0.28	0.41
Ti	0.04	0.11
K	0.01	0.03
O	85.04	82.81

Elem.	At, (%)	Wt, (%)
Si	3.70	5.93
Ca	2.45	5.60
Na	2.77	3.63
Al	0.78	1.20
Fe	0.35	1.11
Mg	0.72	0.99
C	1.23	0.84
Mn	0.19	0.59
O	87.81	80.10

Elem.	At, (%)	Wt, (%)
Si	4.32	6.92
Ca	2.52	5.75
Na	3.31	4.34
C	3.10	2.12
Al	0.98	1.51
Fe	0.28	0.91
Mg	0.45	0.63
Mn	0.11	0.34
O	84.92	77.48

Fig. 10 EDX analysis of 3-day AAM specimen

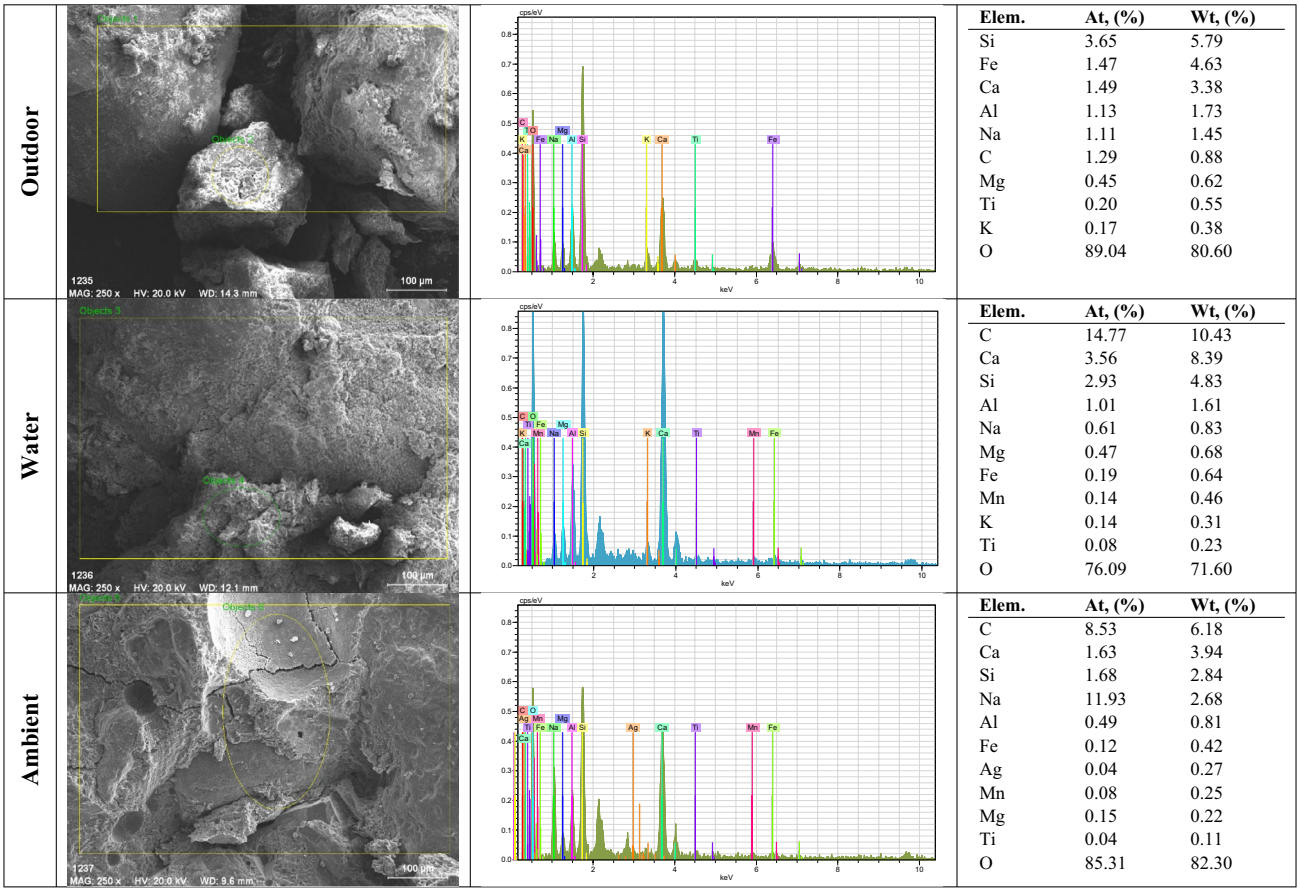
3.4.4 FTIR spectroscopy of AAM specimens

Effects of different curing conditions on the bond structure of 28-day AAMs are presented in Fig. 13. The main absorption bands detected in the AAM samples in the range of approximately 950–1100 cm^{-1} are attributed to characteristic Si–O–Si or Si–O–Al asymmetric stretching vibrations. The pronounced bands in 15-A and 15-W samples prove that ambient conditions and water curing techniques create a suitable environment for the development of bond structures. Similarly, it was reported that the main bands of the spectrum in the AAMs in the range of 900–1000 cm^{-1} indicate the formation of reaction products [31, 48]. FTIR analysis supported the formation and maturity of geopolymer gel phases. It confirmed microstructural observations and compressive strength findings. Additionally, the 1600 cm^{-1} band is generally attributed to H–O–H bending vibrations and this band shows the presence of water molecules. The weakening of this band is due to the dehydration of the matrix [17].

3.5 Effect of specimen dimensions and curing conditions on elevated temperature performance of AAMs

3.5.1 Residual compressive strength

Figure 14 presents the residual compressive strengths of AAM specimens after exposure to 750 °C and their reductions relative to unexposed specimens. Unlike conventional PCC, residual strength increased with specimen dimension across all three curing regimes. This phenomenon may be because small specimens exhibit higher



Elem.	At, (%)	Wt, (%)
Si	3.65	5.79
Fe	1.47	4.63
Ca	1.49	3.38
Al	1.13	1.73
Na	1.11	1.45
C	1.29	0.88
Mg	0.45	0.62
Ti	0.20	0.55
K	0.17	0.38
O	89.04	80.60

Elem.	At, (%)	Wt, (%)
C	14.77	10.43
Ca	3.56	8.39
Si	2.93	4.83
Al	1.01	1.61
Na	0.61	0.83
Mg	0.47	0.68
Fe	0.19	0.64
Mn	0.14	0.46
K	0.14	0.31
Ti	0.08	0.23
O	76.09	71.60

Elem.	At, (%)	Wt, (%)
C	8.53	6.18
Ca	1.63	3.94
Si	1.68	2.84
Na	11.93	2.68
Al	0.49	0.81
Fe	0.12	0.42
Ag	0.04	0.27
Mn	0.08	0.25
Mg	0.15	0.22
Ti	0.04	0.11
O	85.31	82.30

Fig. 11 EDX analysis of 28-day AAM specimens

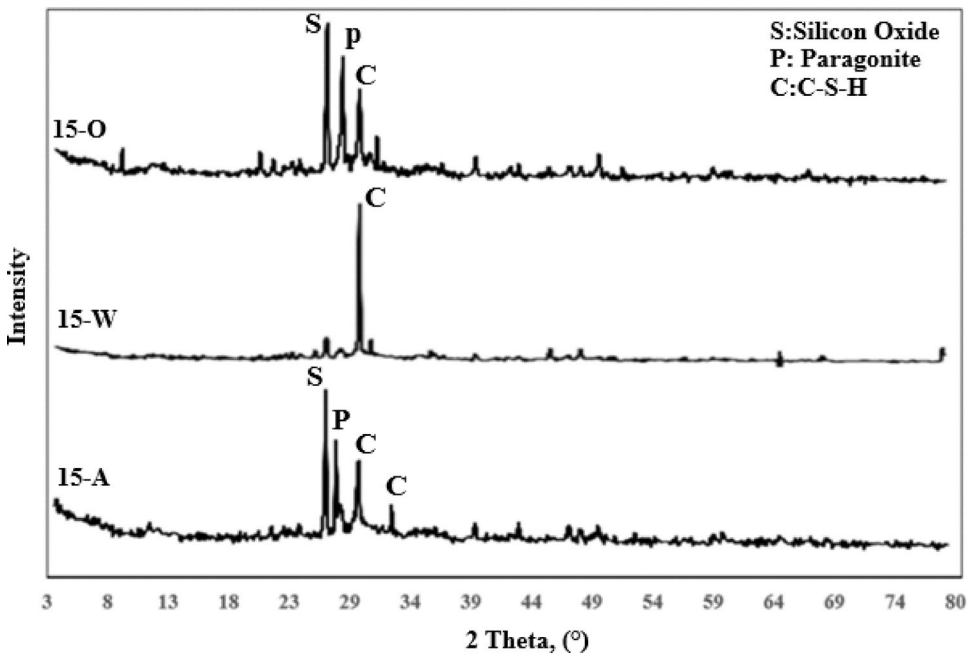


Fig. 12 XRD analysis of 28-day AAM specimen

 https://doi.org/10.1007/s43452-026-01540-3

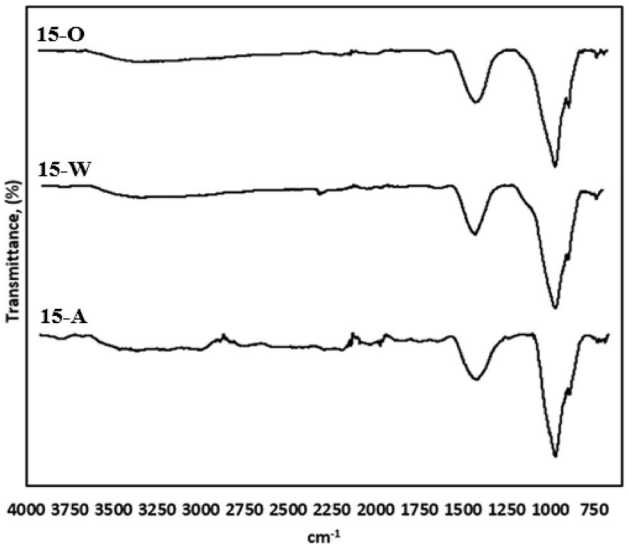


Fig. 13 FTIR analysis of 28-day AAM specimens

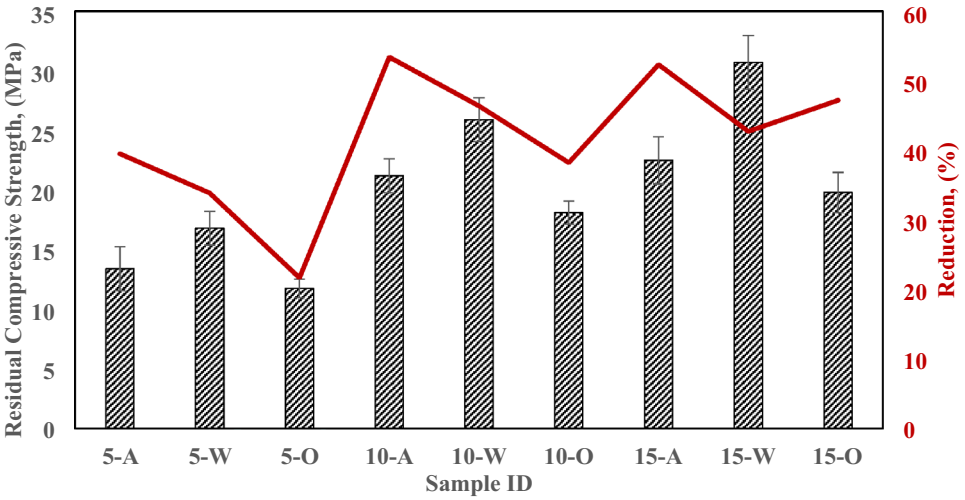


Fig. 14 Residual compressive strengths of AAM specimens

thermal conductivity, leading to increased internal vapor pressure and sudden expansions, thereby promoting crack formation. In small samples, the chemical decomposition of the binder phase was more rapid due to faster and more intense penetration of high temperature into the inner parts [35]. In large samples, slower and later heating of the inner regions leads to a lower thermal gradient. This allows the vapor pressure to dissipate more gradually, leading to lower thermal stresses and reducing microstructural damage in the inner regions [21]. Maximum residual compressive strength for all three specimen dimensions was observed in the water-cured samples. The lowest compressive strengths were recorded in outdoor-cured specimens. Water curing promotes C–S–H-like phases in high-calcium GGBFS-based AAMs, fostering a denser internal structure with better resistance to thermal degradation [14]. In outdoor cured AAM samples, low ambient temperatures slowed down the alkali activation mechanism, resulting in a weaker bond structure and therefore lower residual compressive strength. Curing under laboratory conditions, characterized by constant temperature and humidity, resulted in a moderate and balanced strength development.

3.5.2 Weight loss

The weight losses of AAMs after elevated temperatures are graphically presented in Fig. 15. An increase in specimen dimension led to a increase in weight loss. In larger specimens, the delayed heat penetration into the

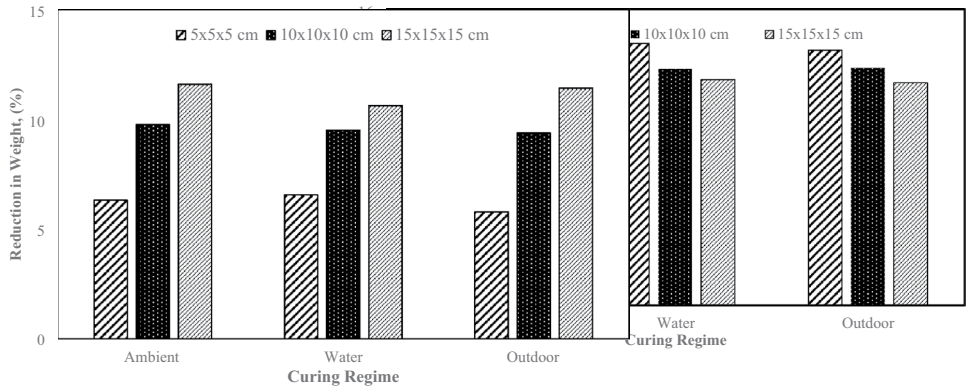


Fig. 15 Weight loss of AAM specimens

Fig. 16 Water absorption values of AAMs

inner regions led to increased internal pressure. This increased internal pressure might lead to thermal damage and higher weight loss (Kong and Sanjayan 2008). It was determined that AAM specimens of identical dimension exhibited similar weight losses after exposure to high temperatures, regardless of the curing condition. The weight losses over 750 °C occur because of the decomposition of carbonate species [19].

3.5.3 Change in water absorption

The water absorption values of AAMs after elevated temperatures are graphically shown in Fig. 16. The water absorption after subjected to 750 °C reveal a consistent decline with increasing specimen dimension. This trend is associated with the decreasing SA/V ratio in larger specimens. It is attributed to the lower degree of heating in

Table 7 Visual appearances of the AAM samples before and after elevated temperature

Curing Condition	Unexposed samples	Samples exposed to 750 °C
Ambient		
Water		
Outdoor		

the inner regions of larger AAM specimens, resulting in fewer cracks and reduced porosity [51]. The maximum water absorption was obtained in the small sample (5-W) cured in water. This might be attributed to the fact that the water curing process causes more moisture absorption during the setting and hardening, thus creating more capillary spaces and open pores.

3.5.4 Visual appearance

Visual appearances of the AAM samples before and after elevated temperature exposure are exhibited in Table 7. The visual appearance changes are related to the physical and chemical effects of elevated temperatures. A distinct colour change was observed in AAM samples exposed to 750 °C. The visual appearance appeared as a shift to yellowish-beige tones and superficial colour irregularities, particularly in ambient-cured and outdoor-cured AAM samples. This is attributed to the dehydration, thermal decomposition and deterioration of crystal structures in geopolymer gel [21], [15]. In water-cured AAM samples, a homogeneous colour and surface texture was observed. Water curing created a dense and stable microstructure, thus providing resistance to thermal deterioration [35]. Cracks and superficial spalling observed after elevated temperature were pronounced in outdoor-cured AAM samples. Surface cracks and crumbling in geopolymer mortar samples occur due to thermal expansion differences, internal pressure increase and weakening of the bond structure [26].

3.5.5 Microstructure

3.5.5.1 SEM analysis After exposure to elevated temperature, distinct microstructural degradation is evident in all curing regimes (Fig. 17). Figure 17a–c shows that the porous and weak microstructure observed in outdoor cured samples continued after the high temperature effect. This is due to insufficient geopolymerization due to low temperatures at outdoor curing conditions. On the other hand, in water-cured AAM specimens (Fig. 17d–f),

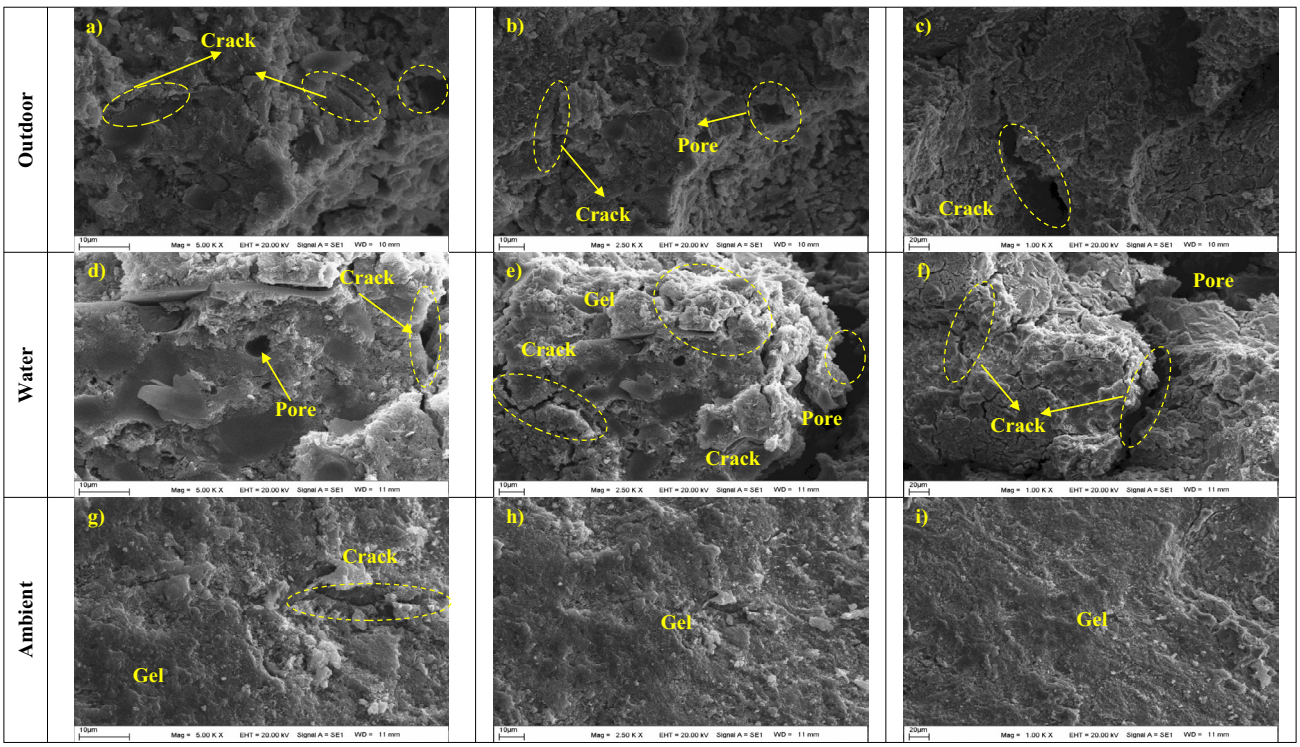
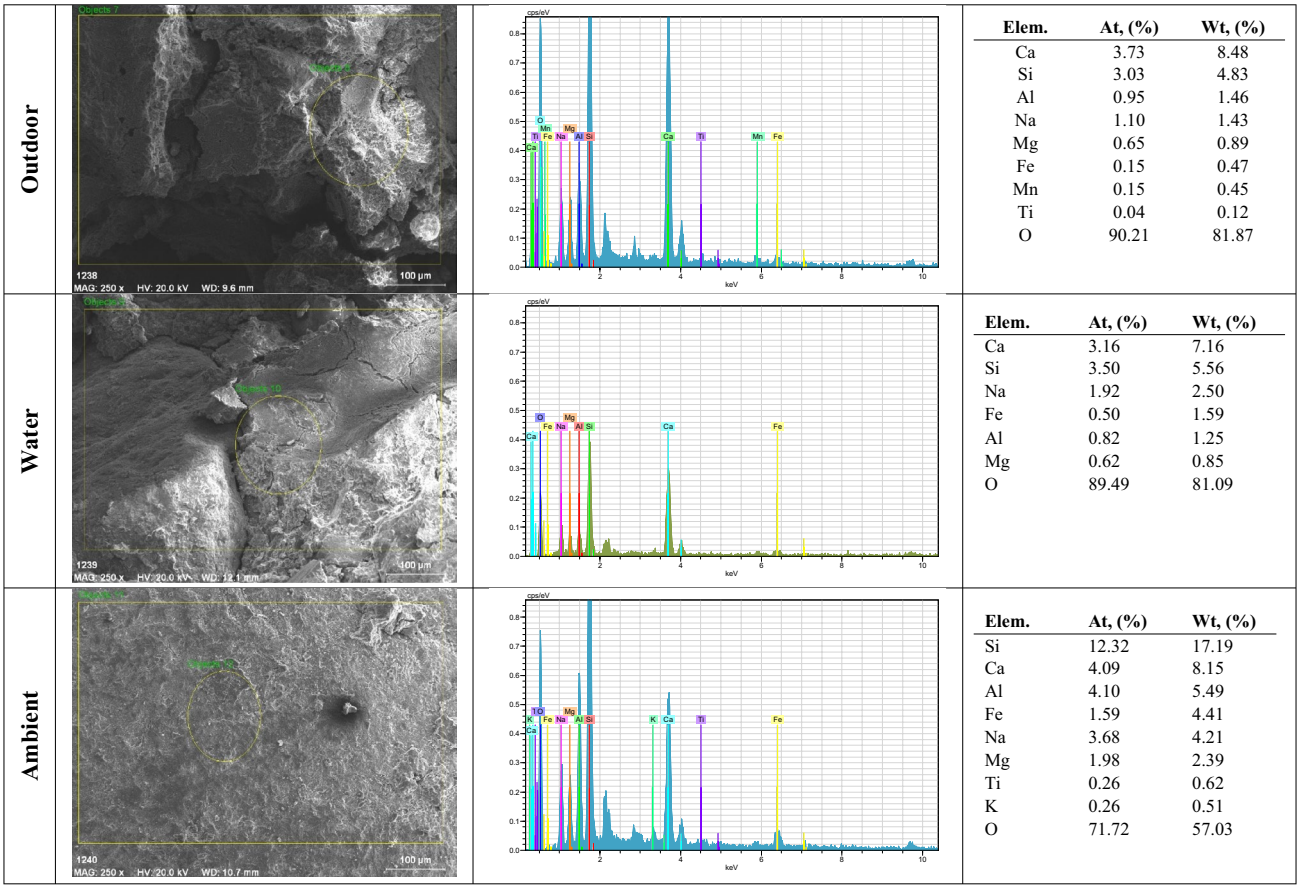


Fig. 17 SEM images of AAM specimens after exposed to elevated temperatures.



Elem.	At, (%)	Wt, (%)
Ca	3.73	8.48
Si	3.03	4.83
Al	0.95	1.46
Na	1.10	1.43
Mg	0.65	0.89
Fe	0.15	0.47
Mn	0.15	0.45
Ti	0.04	0.12
O	90.21	81.87

Elem.	At, (%)	Wt, (%)
Ca	3.16	7.16
Si	3.50	5.56
Na	1.92	2.50
Fe	0.50	1.59
Al	0.82	1.25
Mg	0.62	0.85
O	89.49	81.09

Elem.	At, (%)	Wt, (%)
Si	12.32	17.19
Ca	4.09	8.15
Al	4.10	5.49
Fe	1.59	4.41
Na	3.68	4.21
Mg	1.98	2.39
Ti	0.26	0.62
K	0.26	0.51
O	71.72	57.03

Fig. 18 EDX analysis of AAM specimens after exposed to elevated temperatures

despite the previously dense matrix, gel disintegration and thermal microcracks are observed, indicating that fire exposure significantly disrupts the reaction products. It might have formed as a result of excess moisture and excess water absorption of geopolymer matrix. A compact and dense microstructure was observed in ambient-cured AAM specimens. The geopolymerization process under laboratory conditions promoted the formation of dense C–A–S–H like bonding phases, thus increasing thermal stability [42]. Overall, the AAM specimens exhibited minimum crack and void formation, maintaining a high degree of structural integrity after elevated temperature exposure. Additionally, experimental findings revealed that the that curing conditions have a vital influence on the elevated temperature resistance of AAMs.

3.5.5.2 EDX analysis The EDX analysis of AAM specimens is presented in Fig. 18. Detection of Si, Al, and O elements in AAM samples indicates the formation of aluminosilicate structures AAM samples. The irregularity observed in the distribution of these elements in the outdoor cured geopolymer sample is attributed to restricted hydration and low binding capacity [1]. This might lead to lower compressive strength in outdoor cured AAM sample. The presence of Ca, Al, Si, and a low level of Na in the water-cured geopolymer sample proves the presence of C–(N)–A–S–H hybrid gels [32]. This observation is in consistent with the high residual compressive strength values obtained from water-cured AAM specimens. In ambient-cured AAMs, Ca element is not observed, while Na, Al and Si is more pronounced,this is attributed to the presence of N–A–S–H gels [42]. EDX analysis findings reveal the effect of curing conditions on the chemical composition of geopolymer binder phases.

3.5.5.3 XRD analysis Figure 19 presents the XRD analysis of AAM specimens. Gismondine ($CaAl_2Si_2O_8{\cdot}_4H_2O$), silicon oxide ($SiO_2$), trabzonite ($Ca_4(Si_3O_9)(OH)_2$), and quartz ($SiO_2$) phases were detected in the AAM specimens after elevated temperatures. However, gismondine and silicon oxide phases were consistently detected in all AAM specimens regardless of the curing condition. The presence of quartz and silicon oxide peaks in XRD patterns suggests the existence of unreacted siliceous precursors, retained as residual phases within the geopoly-

 https://doi.org/10.1007/s43452-026-01540-3

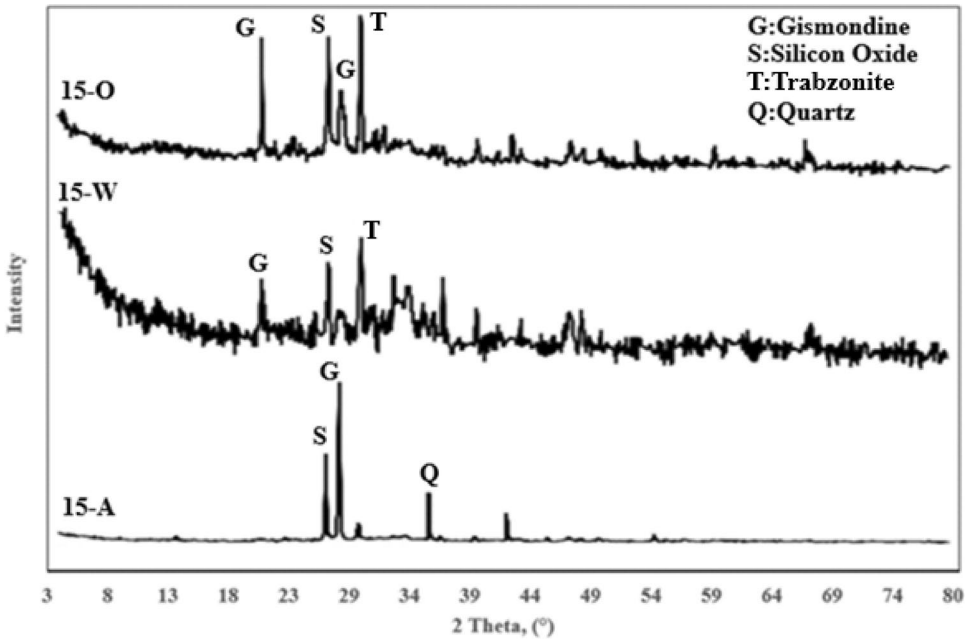


Fig. 19 EDX analysis of AAM specimens after exposed to elevated temperatures

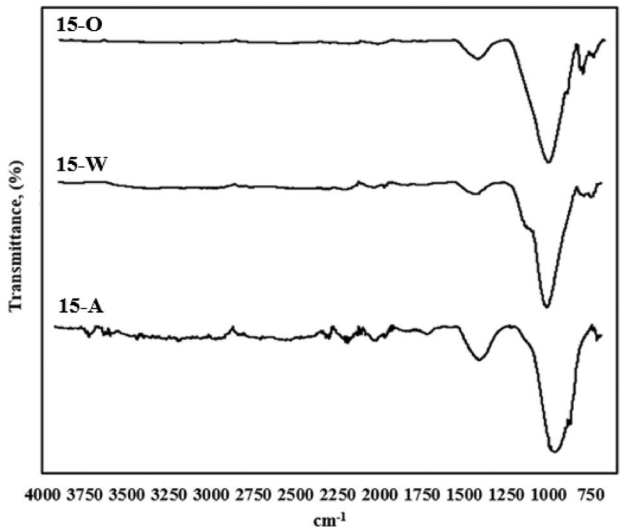


Fig. 20 FTIR analysis of AAM specimens after exposed to elevated temperatures

mer matrix. Gismondine is an aluminosilicate phase that crystallizes under suitable conditions during the alkali activation process and contributes to thermal stability [30].

3.5.5.4 FTIR spectroscopy Figure 20 presents the FTIR analysis of the AAM specimens. The noticeable weakening of the absorption bands at 3300–3450 cm^{-1} (O–H stretching) and 1640 cm^{-1} (H–O–H bending) in the FTIR spectrum shows the effects of dehydration and dehydroxylation after high temperature exposure [19]. Additionally, a broad absorption band was also detected around ~ 960 cm^{-1}. It is attributed to the Si–O–Si and Si–O–Al bonds, in agreement with previous findings reported by Rees et al. [34]. The absorption band observed around 1290 cm^{-1} is attributed to vibrational modifications in aluminosilicate chains, which typically occur during

structural transformations in AAS systems [27]. Disappearance of carbonate-related bands around ~ 1470 cm^{-1} and ~ 870 cm^{-1} confirms the thermal decomposition of carbonates, which typically starts above 400 °C [8, 20].

4 Conclusion

This study systematically investigates the synergistic effects of specimen dimensions and realistic curing conditions on mechanical, physical, microstructural properties and high-temperature performance of AAMs. The key findings of the research are concluded below:

- AAMs with larger dimensions and water-curing conditions exhibited significantly higher compressive strength values compared to smaller AAM specimens cured under outdoor and ambient conditions due to the geopolymerization continuity and microstructural densification.
- Water absorption values of AAMs were influenced by both specimen dimension and curing regime. Small specimens exhibited higher absorption due to their larger SA/V ratios, while water absorption decreased with increasing specimen dimension across all curing regimes.
- Brittle fractures with vertical cracks were observed in larger, water-cured AAM specimens with higher compressive strength, whereas granular fragmentation and irregular fracture surfaces were identified in smaller, outdoor-cured AAM specimens, consistent with their lower compressive strength results.
- Water-cured 15 × 15 × 15 cm AAM samples developed a dense aluminosilicate matrix with fewer cracks and unreacted particles, whereas outdoor-cured specimens retained higher porosity and microcracks, consistent with their lower mechanical performance.
- High Si and Al ratios in 3-day ambient-cured AAM samples suggested early polycondensation, while increased Na, Ca, and Al contents in water-cured specimens supported activator diffusion, formation of C–A–S–H alongside N–A–S–H gels, and the associated strength development.
- Water curing enhanced C–S–H crystallization, whereas ambient and outdoor curing resulted in greater residual silica and paragonite due to incomplete geopolymerization.
- FTIR analysis confirmed the development and maturity of geopolymer gel phases through distinct Si–O–Si and Si–O–Al bands in 15-A and 15-W samples.
- Residual compressive strength of AAM samples after exposure to 750 °C increased with specimen dimension under all curing conditions, and the highest values were obtained in water-cured samples due to the formation of C–S–H-like phases.
- Under all three curing conditions, increasing specimen dimension led to greater weight loss due to delayed heat penetration and the resulting internal pressure buildup that caused thermal damage.
- Water absorption after elevated temperatures decreased with increasing specimen dimension due to lower SA/V ratios and reduced internal cracking.
- After exposure to 750 °C, distinct colour changes, surface cracks, and spalling were observed in AAMs—particularly in ambient and outdoor-cured samples—due to thermal decomposition and internal pressure, whereas water-cured specimens exhibited more homogeneous appearance, indicating enhanced structural stability against thermal degradation.
- After exposure to 750 °C, outdoor-cured AAM samples exhibited a weak and porous microstructure, while water-cured specimens showed signs of dissociation caused by excess moisture.
- Water-cured AAM samples indicated the formation of C–(N)–A–S–H gels, whereas ambient-cured samples showed dominant N–A–S–H gels, and outdoor-cured specimens exhibited irregular elemental distribution due to limited hydration and low binding capacity.
- XRD analysis after high-temperature exposure revealed the formation of gismondine, silicon oxide, trabzonite, and quartz phases depending on curing conditions, with gismondine and silicon oxide consistently present in all specimens, indicating residual unreacted siliceous precursors within the geopolymer matrix.

- FTIR analysis of AAM specimens exposed to 750 °C revealed band attenuations related to dehydration and dehydroxylation, disappearance of carbonate peaks due to thermal decomposition, and shifts in aluminosilicate bonds indicating structural transformations within the geopolymer matrix.

In conclusion, it should be underlined that this comprehensive study offers both practical implications and certain limitations. Experimental findings demonstrate that increasing sample sizes improves the mechanical performance, microstructural integrity, and water absorption properties of AAMs. This suggests that AAMs may be a potential alternative, particularly in the production of large-scale precast elements. Furthermore, the findings regarding the effect of sample size on compressive strength, differing from the classical fracture-mechanics expectations for Portland-cement-based concrete, offered a new perspective to the literature and revealed the unique compressive behavior of geopolymer systems. However, the study's use of GGBFS as the sole binder, activation using only 10 M NaOH solution, and failure to address long-term durability criteria such as freeze–thaw cycles, carbonation, and chemical attack should be regarded as significant limitations. Therefore, future studies designed to address these limitations will significantly contribute to the potential use of AAMs as an alternative in prefabricated element production.

Acknowledgements The authors are grateful to the Inonu University for their financial support for the project (FBA-2025-3893).

Funding Open access funding provided by the Scientific and Technological Research Council of Türkiye (TÜBİTAK).

Data availability Data will be made available on request.

Declarations

Conflict of interest No potential conflict of interest was stated by the authors.

Open Access This article is licensed under a Creative Commons Attribution 4.0 International License, which permits use, sharing, adaptation, distribution and reproduction in any medium or format, as long as you give appropriate credit to the original author(s) and the source, provide a link to the Creative Commons licence, and indicate if changes were made. The images or other third party material in this article are included in the article's Creative Commons licence, unless indicated otherwise in a credit line to the material. If material is not included in the article's Creative Commons licence and your intended use is not permitted by statutory regulation or exceeds the permitted use, you will need to obtain permission directly from the copyright holder. To view a copy of this licence, visit http://creativecommons.org/licenses/by/4.0/.

References

1. Allison PG, Weiss CA, Moser RD, Diaz AJ, Rivera OG, Holton SS. Nanoindentation and SEM/EDX characterization of the geopolymer-to-steel interfacial transition zone for a reactive porcelain enamel coating. Compos B Eng. 2015;78:131–7.
2. ASTM C109. Standard test method for compressive strength of hydraulic cement mortars (using 2-in. or [50 mm] cube specimens). ASTM International; 2021.
3. ASTM C1723. Standard guide for examination of hardened concrete using scanning electron microscopy. ASTM International; 2016.
4. ASTM C642. Standard test method for density, absorption, and voids in hardened concrete. ASTM International; 2013.
5. ASTM E1252. Standard practice for general techniques for obtaining infrared spectra for qualitative analysis. ASTM International; 2021.
6. Bai W, Ye D, Ye S, Yuan C, Guan J, Yang G, et al. Study on mechanical properties and damage mechanism of alkali-activated slag concrete. J Build Eng. 2024;96:110357.
7. Biricik H, Kırgız MS, de Sousa Galdino AG, Kenai S, Mirza J, Kinuthia J, et al. Activation of slag through a combination of NaOH/NaS alkali for transforming it into geopolymer slag binder mortar–assessment the effects of two different Blaine fines and three different curing conditions. J Mater Res Technol. 2021;14:1569–84.

8. Cheng-Yong H, Yun-Ming L, Abdullah MMAB, Hussin K. Thermal resistance variations of fly ash geopolymers: foaming responses. Sci Rep. 2017;7(1):45355.
9. Darvish P, Alengaram UJ, Yap SP, Ibrahim S, Yusoff S. Performance evaluation of palm oil clinker sand as replacement for conventional sand in geopolymer mortar. Constr Build Mater. 2020;258:120352.
10. Durastanti C, Moretti L. Environmental impacts of cement production: A statistical analysis. Appl Sci (Basel). 2020;10(22):8212.
11. Duxson P, Provis JL, Lukey GC, Mallicoat SW, Kriven WM, Van Deventer JS. Understanding the relationship between geopolymer composition, microstructure and mechanical properties. Colloids Surf A. 2005;269(1–3):47–58.
12. Elewa K, Tawfic AF, Tarek M, Al-Sagheer NA, Nagy NM. Removal of methylene blue from synthetic industrial wastewater by using geopolymer prepared from partially dealuminated metakaolin. Sci Rep. 2025;15(1):1–16.
13. Gagg CR. Cement and concrete as an engineering material: An historic appraisal and case study analysis. Eng Fail Anal. 2014;40:114–40.
14. Gebregziabiher BS, Thomas R, Peethamparan S (2015) Very early-age reaction kinetics and microstructural development in alkali-activated slag. Cem con compos 55:91-102
15. He J, Zhang J, Yu Y, Zhang G (2012) The strength and microstructure of two geopolymers derived from metakaolin and red mud-fl y ash admixture: A comparative study. Constr buil mater 30:80-91
16. Ismail I, Bernal SA, Provis JL, San Nicolas R, Hamdan S, van Deventer JS. Modification of phase evolution in alkali-activated blast furnace slag by the incorporation of fly ash. Cement Concr Compos. 2014;45:125–35.
17. Khaliq W, Khan HA. High temperature material properties of calcium aluminate cement concrete. Constr Build Mater. 2015;94:475–87.
18. Khawaji M. Hydration, microstructure, and properties of fly ash-based geopolymer: a review. Mater Sci Pol. 2023;41(2):263–87.
19. Kljajević L, Nenadović M, Ivanović M, Bučevac D, Mirković M, Mladenović Nikolić N, et al. Heat treatment of geopolymer samples obtained by varying concentration of sodium hydroxide as constituent of alkali activator. Gels. 2022;8(6):333.
20. Kloprogge JT, Frost RL, Hickey L. Infrared emission spectroscopic study of the dehydroxylation of some hectorites. Thermochim Acta. 2000;345(2):145–56.
21. Kong DL, Sanjayan JG (2008) Damage behavior of geopolymer composites exposed to elevated temperatures. Cem Concr Compos 30(10):986-991
22. Lancellotti I, Catauro M, Ponzoni C, Bollino F, Leonelli C. Inorganic polymers from alkali activation of metakaolin: effect of setting and curing on structure. J Solid State Chem. 2013;200:341–8.
23. Li Q, Li X, Yang K, Zhu X, Gevaudan JP, Yang C, et al. The long-term failure mechanisms of alkali-activated slag mortar exposed to wet-dry cycles of sodium sulphate. Cem Concr Compos. 2021;116:103893.
24. Liu J, Shi X, Zhang G, Li L. Study the mechanical properties of geopolymer under different curing conditions. Minerals. 2023;13(5):690.
25. Liu C, Li Z, Ye G. Mechanisms of efflorescence of alkali-activated slag. Cem Concr Compos. 2025;155:105811.
26. Luhar S, Chaudhary S, Luhar I. Thermal resistance of fly ash based rubberized geopolymer concrete. J Build Eng. 2018;19:420–8.
27. Marple MA, Koroglu B, Morrison K, Crowhurst J, Balachandra A, Soroushian P, et al. Accelerated carbonation and structural transformation of blast furnace slag by mechanochemical alkali-activation. Cem Concr Res. 2022;156:106760.
28. Mokhtar A, Nasooti M. A decision support tool for cement industry to select energy efficiency measures. Energy Strategy Rev. 2020;28:100458.
29. Nuruddin MF, Malkawi AB, Fauzi A, Mohammed BS, Almattarneh HM. Geopolymer concrete for structural use: Recent findings and limitations. In: IOP conference series: materials science and engineering (Vol. 133, No. 1). IOP Publishing; 2016. p. 012021.
30. Okoronkwo MU, Mondal SK, Wang B, Ma H, Kumar A. Formation and stability of Gismondine-type zeolite in cementitious systems. J Am Ceram Soc. 2021;104(3):1513–25.
31. Puligilla S, Mondal P. Co-existence of aluminosilicate and calcium silicate gel characterized through selective dissolution and FTIR spectral subtraction. Cem Concr Res. 2015;70:39–49.
32. Provis JL, Van Deventer JSJ (Eds.) (2009) Geopolymers: structures, processing, properties and industrial applications. Elsevier
33. Rashad AM, Zeedan SR, Hassan AA. Influence of the activator concentration of sodium silicate on the thermal properties of alkali-activated slag pastes. Constr Build Mater. 2016;102:811–20.
34. Rees CA, Provis JL, Lukey GC, van Deventer JS. Attenuated total reflectance Fourier transform infrared analysis of fly ash geopolymer gel aging. Langmuir. 2007;23(15):8170–9.
35. Rickard WD, Riessen AV, Walls P. Thermal character of geopolymers synthesized from class F fly ash containing high concentrations of iron and α-quartz. Int J Appl Ceram Technol. 2010;7(1):81–8.
36. Ríos JD, Vahí A, Leiva C, Martínez-De la Concha A, Cifuentes H. Analysis of the utilization of air-cooled blast furnace slag as industrial waste aggregates in self-compacting concrete. Sustainability (Basel). 2019;11(6):1702.

37. Saludung A, Azeyanagi T, Ogawa Y, Kawai K. Mechanical and microstructural evolutions of fly ash/slag-based geopolymer at high temperatures: effect of curing conditions. Ceram Int. 2023;49(2):2091–101.
38. Shi C, Jiménez AF, Palomo A. New cements for the 21st century: the pursuit of an alternative to Portland cement. Cem Concr Res. 2011;41(7):750–63.
39. Sonebi M, Ammar Y, Diederich P. Sustainability of cement, concrete and cement replacement materials in construction. In: Sustainability of construction materials. Woodhead Publishing; 2016. pp. 371–96.
40. Soomro M, Tam VW, Evangelista ACJ. Production of cement and its environmental impact. In: Recycled concrete. Woodhead Publishing; 2023. pp. 11–46.
41. Sun B, Ye G, De Schutter G. A review: reaction mechanism and strength of slag and fly ash-based alkali-activated materials. Constr Build Mater. 2022;326:126843.
42. Temuujin J, van Riessen A, Williams R. Influence of calcium compounds on the mechanical properties of fly ash geopolymer pastes. J Hazard Mater. 2009;167(1–3):82–8.
43. TS EN 1008. Mixing water for concrete-specifications for sampling, testing and assessing the suitability of water, including water recovered from processes in the concrete industry, as mixing water for concrete. Turkish Standards Institution; 2003.
44. TS EN 1097–6. Tests for mechanical and physical properties of aggregates—Part 6: determination of particle density and water absorption. Turkish Standards Institution; 2022.
45. TS EN 197-1. Cement-Part 1: composition, specifications and conformity criteria for common cements. Turkish Standards Institution; 2012.
46. Van Deventer JS, Provis JL, Duxson P. Technical and commercial progress in the adoption of geopolymer cement. Miner Eng. 2012;29:89–104.
47. Verma M, Meena RK, Khan MI, Khatib JM. Analysis of the effect of curing and mixing periods on mechanical properties of the geopolymer composite. Mater Sci Pol. 2024;42(4):131–47.
48. Wang Y, Han F, Mu J. Solidification/stabilization mechanism of Pb (II), Cd (II), Mn (II) and Cr (III) in fly ash based geopolymers. Constr Build Mater. 2018;160:818–27.
49. Xue C, Sirivivatnanon V, Nezhad A, Zhao Q. Comparisons of alkali-activated binder concrete (ABC) with OPC concrete-A review. Cem Concr Compos. 2023;135:104851.
50. Zhang S, Li Z, Ghiassi B, Yin S, Ye G. Fracture properties and microstructure formation of hardened alkali-activated slag/fly ash pastes. Cem Concr Res. 2021;144:106447.
51. Zhao J, Wang K, Wang S, Wang Z, Yang Z, Shumuye ED, et al. Effect of elevated temperature on mechanical properties of high-volume fly ash-based geopolymer concrete, mortar and paste cured at room temperature. Polymers. 2021;13(9):1473.

Publisher's Note Springer Nature remains neutral with regard to jurisdictional claims in published maps and institutional affiliations.

Authors and Affiliations

Enes Ekinci[1] · Fatih Kantarcı[1]

✉ Fatih Kantarcı
fatih.kantarci@inonu.edu.tr

Enes Ekinci
enes.ekinci@inonu.edu.tr

[1] Department of Civil Engineering, Faculty of Engineering, İnönü University, 44280 Malatya, Turkey